2022 IEEE/SICE International Symposium on System Integration (SII)
January 9-12, 2022. Narvik, Norway

2022 IEEE/SICE International Symposium on System Integration (SII) | 978-1-6654-4540-5/22/$31.00 ©2022 IEEE | DOI: 10.1109/SII52469.2022.9708750

Design of A High Strength Multi-Steering Climbing Robot for Steel Bridge Inspection

Cadence Motley, Son T. Nguyen, Hung M. La, *IEEE Senior Member*

***Abstract*— The Advanced Robotics and Automation (ARA) Lab has engineered its next-generation robot for steel bridge inspection. This particular design is specialized for its particularly high strength adhesion force and high maneuverability. The robot can utilize various steering configurations such as Ackermann, synchronous and static point steering while navigating steel structures and adhering to cylindrical members. The adhesion system creates a comprehensive platform for adding extra sensing equipment by the user and will serve as a basis for future works. This paper will discuss in detail the design work done to ensure that the proposed robot would function as intended before we made it and show how the capabilities we engineered the proposed robot have made it a step forward for the steel inspection industry.**

I. Introduction

Steel bridge inspection is a dangerous job, which requires in-depth training on safe practices and knowledge about overall bridge and steel condition assessment [1]. This job often requires people to enter very tight spaces between members or hang beneath the bridge. As a result, performing a bridge inspection can be extremely dangerous, costly, and time-consuming. Work should be done to create robotics [2], [3] that can dramatically assist inspectors in improving the safety of conducting steel bridge inspections.

The Advanced Robotics and Automation (ARA) Lab here at the University of Nevada, Reno (UNR), with funding from the National Science Foundation (NSF) and the federal Department of Transportation (DoT), has been researching the application of robotics to improve the safety around conducting inspections. This paper introduces the next generation of one of the proposed robots and the mathematics and methods behind its design. We also layout and discuss two of our newest analyses for creating mobile robots on steel bridges.

In the United States, there are 175,825 bridges containing major steel components [4]. In a recent report put out by the American Society of Civil Engineers in 2016, they found that "9.1% of the nation's bridges were structurally deficient" [5]. Part of this can be attributed to America's aging infrastructure and has far-reaching consequences should failure occur in a bridge. America's roadways are a part of the backbone of our economy, and bridges often serve a significant role in them since they path over rugged terrain that would not be passable otherwise.

In 2007 the I-35W bridge over the Mississippi River in Minnesota collapsed unexpectedly, resulting in the death of 13 people and the injury of another 145. In addition to the damage and loss of life, the economic impact was estimated to be a net loss of $120,000 per day by the Minnesota Truckers Association [6]. To mitigate the tremendous cost of unexpected failure, work should be done to improve the safety, detail, and efficiency of steel bridge inspections.

There are a variety of recent works within the field of steel bridge inspection robots. Some of these take surface-based approaches, and others take aerial ones. We will focus on surface-based solutions since the proposed robot is a surface-based solution as well.

CROC [7] and the hybrid climbing robot [8] feature the ability to move around in an inch worm-like manner. While these robots have a great potential to move around and adhere to a wide variety of areas, these robots suffer from being very complicated to control. The control frameworks needed to utilize these robots efficiently are computationally expensive and require much power. This is particularly disadvantageous since the operation of these robots occurs in hard-to-reach areas on steel bridges where power is not as accessible as it would be in other areas.

MINOAS [9] and BIREM [10] are smaller steel inspection robots. They both work for their intended purpose but cannot bear additional weight to do anything more than gather visual data. When inspecting steel, surface-level data is not enough to properly provide a good quality inspection of a steel section. This means that these robots do not eliminate the need for inspectors to physically go to the areas the robot observes.

Another recent work by Helical Robots created a robot for inspection of wind turbine towers [11]. However, the robot cannot transfer from the tower to the generator or to still blades because it generates its magnetic adhesion force at its center. This causes the robot to be unable to transfer between surfaces. Some other developments are [12] and [13]. Despite flexible locomotion, these robots cannot carry high loads because of limited contact between the robot's wheels and surfaces.

The robot proposed in this paper (Fig. 1) takes a wheeled approach with a much larger adhesion system on board.

This work is supported by the U.S. Department of Transportation, Office of the Assistant Secretary for Research and Technology (USDOT/OST-R) under Grant No. 69A3551747126 through INSPIRE University Transportation Center, and the U.S. National Science Foundation (NSF) under grants NSF-CAREER: 1846513 and NSF-PFI-TT: 1919127. The views, opinions, findings and conclusions reflected in this publication are solely those of the authors and do not represent the official policy or position of the NSF and USDOT/OST-R.

The authors are with the Advanced Robotics and Automation (ARA) Lab, Department of Computer Science and Engineering, University of Nevada, Reno, NV 89557, USA. Corresponding author: Hung La, email: hla@unr.edu.

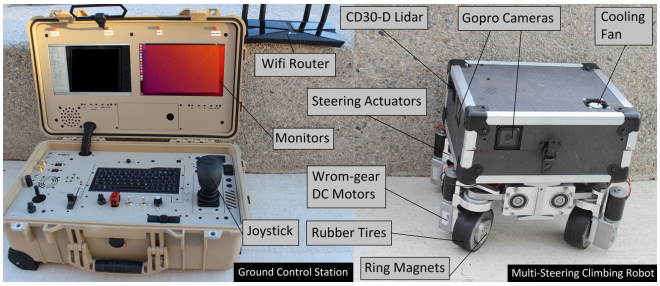

Fig. 1: The Ground Control Station (GCS) performs localization, object detection and visualizes the received data online on its two screens. We use an Intel NUC i7 as the computer for the GCS.

This system allows the proposed robot to travel over $90°$ edges and to new steel surfaces. The unique ring magnet wheels make the proposed robot capable of carrying very large equipment loads and allow the proposed robot to be outfitted with lots of additional sensing equipment and sensors. The adhesion system is supplemented with excellent steering capabilities with the four independent wheel sub-assemblies, allowing the proposed robot to have a high degree of steerability and maneuverability on steel surfaces. This system enables the proposed robot to efficiently hit specific positions and orientations to maximize the robot's ability to utilize onboard equipment. The proposed robot also can travel on curved surfaces. These features combined into one compact robot allow for and create a generally more capable robot than other recent works that can be applied in the broader degree of settings for research purposes.

II. Overall Design

The design has a chassis made of an aluminum I-beam and four modular wheel sub-assemblies attached to it, as shown in Fig. 2 & 3. Different from our previous design [14], each of wheel sub-assemblies is completely independent to allow the robot to utilize different steering methods to travel along a surface. We decided that making each wheel independently steerable was the best way to develop a robot that could accurately travel along and between steel surfaces for inspection. This function is meaningful when the robot maneuvers in limited spaces or localize exact positions for sensor deployment. The wheels consist of a large ring magnet and two steel rims on each side.

The robot can traverse long continuous steel surfaces commonly found on steel bridges. With the robot's ability to take advantage of different steering configurations, the proposed robot is significantly more capable of reaching precise locations with particular orientations. This allows the robot to utilize onboard inspection equipment more effectively since it has an excellent capacity to modify its heading. The steering modes also give the robot's controller additional methods to interact and move the robot most intuitively.

The ARA Lab robot is capable of traveling through internal and external edges on steel structures and has a spatial footprint of $33cm$ by $22.65cm$ by $30.38cm$ (width, depth, height) as shown in Fig. 2. The wheels have a diameter of $7.62cm$ and width of $3.55cm$. The robot weighs $18.14kg$.

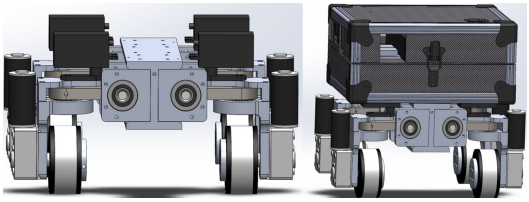

Fig. 2: CAD Model of the Designed Robot.

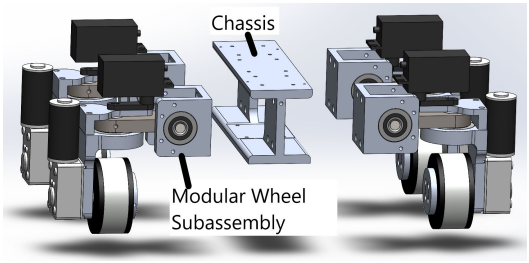

Fig. 3: Exploded CAD Model showing distinction between Modular Wheel Subassemblies and the Chassis.

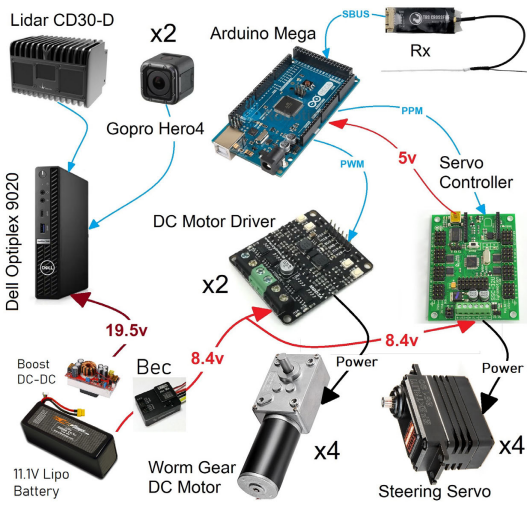

Fig. 4: The electric system on the robot: There are two independent channels of robot teleoperation and monitoring. A Dell Optiplex computer processes the data from Lidar and cameras then is transferred to Ground Control Station (GCS) for live monitoring. For remote control, Rx receives commands from the operator via the GCS's joystick. An Arduino Mega processes these signals and then exports outputs to control the four robot's worm gear motors and four steering servos via power amplifiers.

The analysis section of the paper will discuss the minutiae behind the development of the proposed robot and how its design brings something new to the steel inspection industry. The following analyses have been done: Robot Maneuverability, Turn Over Analysis, Static Contact Stress Analysis, Sliding Friction Analysis, Edge Obstruction Analysis, and a Wheel Steering Analysis. Next, we will talk about the field deployment of the robot and then conclude our paper.

III. Analysis of Robot Design

A. Robot Maneuverability

The engineered robot has been designed with a conventional approach to robotic kinematics [15]. The pro-

posed robot has been designed to have four independently steerable magnetic wheels. This configuration of wheels allows the proposed robot to take advantage of a variety of advantageous steering configurations such as Ackermann, Synchronous, and Static-Point Steering.

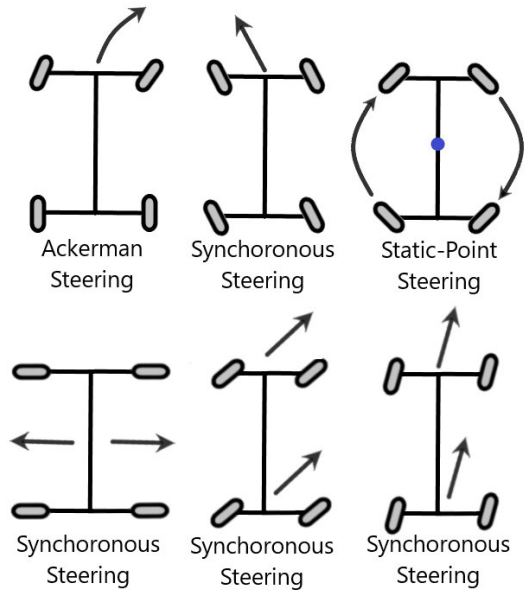

Fig. 5: Steering Configurations.

These allow the proposed robot to be particularly adept at navigating awkward and uneven terrain found on steel structures through its ability to utilize each of the steering types shown in Fig. 5.

Per Muir's approach in their paper with eqs. 3.40, 3.41 and 3.42 [15], the proposed robot's degree of mobility (δ_m), steerability (δ_s) and maneuverability (δ_M) can be determined.

$$\delta_m = 3 - rank[C_1(\beta_s)]. \tag{1}$$

$$\delta_s = rank[C_{1s}(\beta_s)]. \tag{2}$$

$$\delta_M = \delta_m + \delta_s. \tag{3}$$

The C matrix represents the robot's constraints, and β_s is a vector that describes the steering angles of each of the robot's wheels.

With proper control mechanisms, it can be ensured that each of the axes of the wheels intersects at one point, creating an instantaneous center of rotation (ICR). This is the point at which the robot will pivot around while moving. When this condition is met, the proposed robot has a degree of mobility of one, a degree of steerability of two, which results in the proposed robot scoring a three in its degree of maneuverability. This means the ICR of the proposed robot is not constrained to any point on the surfaces it navigates upon.

B. Turn Over Analysis

To ensure that the proposed robot would perform as intended, we have analyzed the proposed robot's mechanical properties and interactions in various scenarios to verify that it will serve as intended. All analyses from here on will build off of previous analyses [8] so it is important that at least a basic understanding is obtained before moving on.

A turn-over analysis is done to ensure that the proposed robot does not topple over and off a steel surface at any point while operating. This analysis considers the two primary orientations in which the robot would be the most susceptible to this type of failure mechanic. The first is a vertical orientation when traveling up a vertical steel beam ($d_2 = 22.65cm$), and the second is a horizontal position when the robot travels along a horizontal steel beam ($d_2 = 33.02cm$).

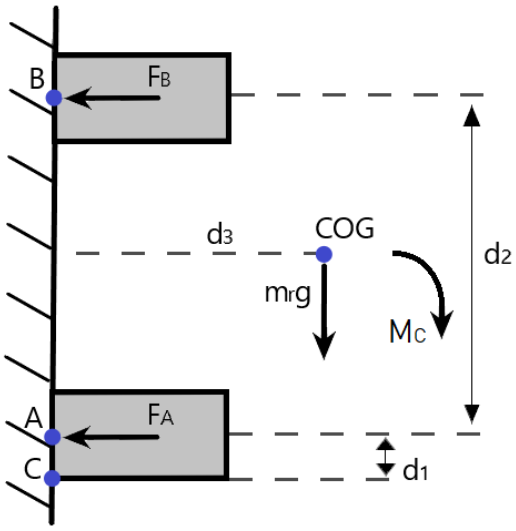

Fig. 6: Turn Over Diagram.

We assume static conditions [$\sum_{i=1}^{n} F_i = 0$, $\sum_{i=1}^{n} M_i = 0$] and take a moment at point C in Fig. 6 (F_i is the adhesive force of i_{th} wheel, M_i is the torque at point C by F_i) to calculate the moment that the magnets are generating in the robot's structure, and how much additional equipment load (M_C) they can withstand before a turn-over failure would occur.

$$M_C = d_1(2F_{Amag}) + (d_1 + d_2)(2F_{Bmag}) - d_3 m_r g, \tag{4}$$

where, d_1 is half the width of the wheels, d_2 is the distance between the centers of the two sets of wheels, d_3 is the height of the center of mass of the robot at which $d_3 = 16.51cm$, F_{Amag} = F_{Bmag} = $400N$, g is the acceleration due to gravity, and m_r is the center mass of the robot.

So as long as M_C is not negative, we can calculate the maximum additional equipment weight m_e that the robot can withstand.

$$m_e = \frac{M_C}{d_3 g}. \tag{5}$$

If M_C was negative, Equ. (5) would tell us how much mass we need to remove to prevent a turn-over failure (M_C = 180.14 Nm).

We engineered the proposed robot to be particularly robust against this type of failure since failure would likely result in

complete loss/destruction of the robot in the instance that it fell from a bridge. The proposed robot is mathematically capable of carrying an additional equipment load of $111.22kg$ for this analysis's failure. This gives it a Factor of Safety (FOS) of 6.13 without additional equipment, which means that failure from turning over should almost never occur at base conditions.

C. Static Contact Stress Analysis

A static contact stress analysis informs us about how our wheels will be interacting with the surfaces they come into contact with. This analysis gives our team information about how much force each wheel will have to go through it. To start, a summation of forces is done assuming static conditions.

$$0 = 2F_{Amag} + 2F_{Bmag} - 2F_A - 2F_B, \tag{6}$$

where F_A and F_B are the reaction forces acting at points A and B in Fig. (6), respectively. We can use Equ. (6) by solving it for F_A and plugging that equation into Equ. (7).

$$\begin{aligned} 0 = 2d_1F_{Amag}) + 2(d_1 + d_2)2F_{Bmag} - d_3m_rg \\ -d_1F_A + (d_1 + d_2)F_B. \end{aligned} \tag{7}$$

Equ. (7) is created by assuming static conditions and taking a moment at C. Since the summation of all moments is equal to zero we are now considering the reactionary forces to create this scenario. From here, we plug Equ. (6) into Equ. (7) and solve for F_B. To get F_A we can now plug our value for F_B into Equ. (6).

$$F_B = \frac{d_2F_{Bmag} - d_3m_rg}{d_2}. \tag{8}$$

We now solve for F_B in Equ. (8) to determine the reaction force acting at point B and subsequently point A with Equ. (6) ($F_A = 529.72$ N). With the reaction forces now known values, we can move on to determine the half-width (b) of the contact area of the wheels caused by the reaction forces acting on them in the normal direction.

$$b = \sqrt{\frac{4F(\frac{1-\nu_1^2}{E_1} + \frac{1-\nu_2^2}{E_2})}{\pi L(\frac{1}{R_1} + \frac{1}{R_2})}}. \tag{9}$$

In Equ. (9), L is the width of the wheel, ν is Poisson's ratio of a material, E is the modulus of elasticity of the material [16], [17] and F is F_A, which is the highest reactionary force acting on any of the wheels for all cases. To create the scenario of a plate (steel surface with subscript [$_2$]) in contact with a cylinder (rubber coated wheels with subscript [$_1$]), R_2 is set to be infinity, creating the scenario a flat surface in contact with a cylinder (this term goes to zero and is therefore dropped). With the half-width, we can now calculate the contact stress on the wheels ($E_r = 0.01$ GPa, $\nu_r = .496$, $E_s = 205$ GPa, $\nu_s = .29$ and $b = .738cm$).

$$p_{max} = \frac{2F}{\pi Lb}. \tag{10}$$

If p_{max} is greater than the compression strength of the structural material within the wheels ($\sigma_{rubber} = 22.5$ MPa) [18], the wheels will be unable to withstand the forces exerted on them by the reaction forces. Based on our calculations, we determined that the SBR rubber-coated steel rims would fit our requirements best with the added benefit of helping to concentrate the magnetic field of the ring magnets through the steel and giving a high friction coefficient. ($p_{max} = 1.285$ MPa).

D. Sliding Friction Analysis

To determine the amount of sliding friction holding the proposed robot in place, we need to solve the net normal force acting on the system distributed between each of the wheels.

$$N = 2F_{Amag} + 2F_{Bmag} + (m_r + m_e)gcos(\theta). \tag{11}$$

Equ. (11) builds off of Equ. (6) except we are no longer assuming that the robot is positioned parallel to the force of gravity. This causes an additional term to appear in the equation to account for the effect of the robot's mass ($m_r + m_e$) and orientation (θ). (Note that N represents the reactionary forces acting to resist the other forces of the system, this is why the F_A and F_B terms are not present since they are now encompassed by N in the system). Now that the normal force has been solved, the next step is to empirically calculate the friction factor (μ) of the rubber-coated wheels with steel ($N(\theta = 90) = 1422.05$ N).

$$\mu = tan(\theta_1). \tag{12}$$

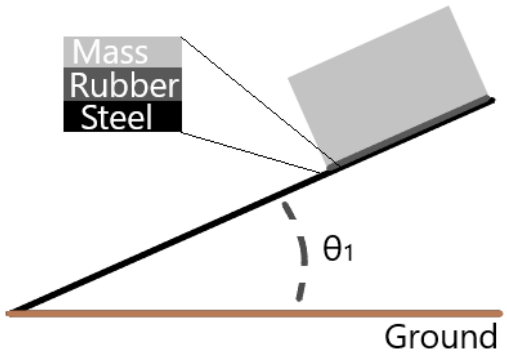

Fig. 7: Friction Factor Test Setup.

The friction factor between two materials can be solved for by setting up a small experiment in which both materials are put into contact with one another and a small mass pushing them together. In our case, we got a block with the rubber coating adhered to one side and a steel beam. By raising one end of the steel beam and a device to measure the angle of it. θ_1 can be determined when the block with the rubber coating on its face begins to slide. Using 30 trials and Equ. (12), we determined that θ_1 is 35° and therefore that, $\mu = 0.7$.

$$F_F = N\mu - (m_r + m_e)g|sin(\theta)|. \tag{13}$$

With the normal force calculated and the friction factor between the two surfaces, the force of friction generated by

the robot can be determined using Equ. (13). We consider both worst case scenarios for the orientation of the robot were $\theta = 90°$ and $\theta = 180°$ (based on the unit circle).

$$m_e = \frac{N\mu}{g} - m_r, \theta = 90°. \tag{14}$$

$$m_e = \frac{2F_{Amag} + 2F_{Bmag}}{g} - m_r, \theta = 180°. \tag{15}$$

Equations (14 and 15) are derived by setting the value of θ and setting $F_F = 0$ to solve for the maximum equipment load for each scenario ($m_e(\theta = 90°) = 96.03$ kg and $m_e(\theta = 180°) = 144.95$ kg). Based on these values, our team was able to determine that the limiting factor in our design was the sliding friction scenario where $\theta = 90°$ and that the proposed robot would not have a traction based issue while on steel.

E. Edge Obstruction Analysis

This analysis is conducted to calculate the necessary motor torque when the robot stands the highest load. It is when the robot passes an internal corner between two perpendicular surfaces (Fig. 8), the front wheel bears an additional force $F_{2.2}$, which is the adhesive force of the front wheel on the surface 2. Similarly, $F_{2.1}$ is the adhesive forces of the front wheel on the surface 1. F_{f2} is the friction of the front wheel on the surface 2, r is the wheel's radius, and k is the static friction coefficient (between rubber and steel in our design). The minimum force of the front wheel that allows the robot to be able to overcome the corner must satisfy:

$$\frac{M_{\text{moving}}}{r} > F_{2.1} + F_{f2} + \frac{P}{2}. \tag{16}$$

Therefore, the moving motor torque needs to satisfy:

$$M_{\text{moving}} > r(F_{2.1} + kF_{2.2} + \frac{P}{2}). \tag{17}$$

In practice, the actual torque is selected to be at least double that of theoretical calculation in (17).

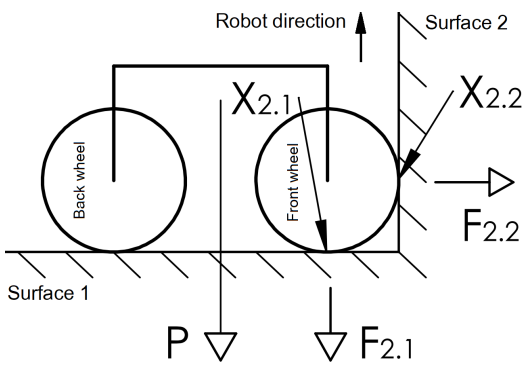

Fig. 8: When the robot passes an internal corner between two perpendicular surfaces, the robot's load increases significantly.

F. Wheel Steering Analysis

Since the proposed robot can steer each of its wheels independently, we needed to create a new analysis to analyze the torque required to turn the wheels in a given moment. Since static friction is greater than kinetic friction, we assume that the robot is stationary when it turns its wheels. At any instant, the wheels have a contact line with the surfaces they are on and a point at which the center of rotation (CR) occurs when steering. The robot's wheels have been designed to have a center of rotation at the center of the width of the wheel. This has been done to minimize our steering servos' required output torque and reduce steering complexity from the case of castor-like wheels.

$$M(x) = \int_a^b V(x)dx. \tag{18}$$

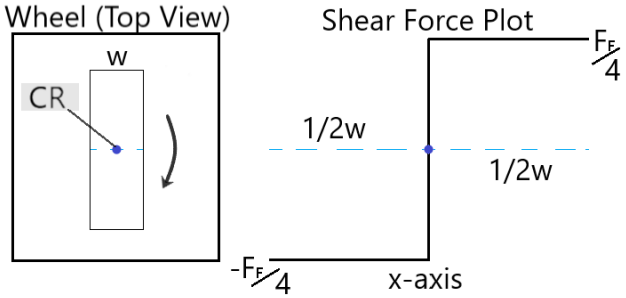

Fig. 9: [left] A top down view of a wheel with width (w), which is rotating about point CR. [right] Shear force diagram along the wheels contact line.

Drawing on insights from Euler-Bernoulli beam theory [19] on the relationships between shear forces and moments, we can write Equ. (18). We create a shear force (V) diagram about the contact line as shown on the right side of Fig. (9) with a magnitude of $\frac{F_F}{4}$ where x is the distance along the contact line from the center of rotation.

$$V(x) = \frac{F_F}{4}. \tag{19}$$

The force of friction in Equ. (19) always acts in opposition to the wheel's rotation and is a constant since the robot is stationary.

$$M_{CR} = \frac{F_F w}{4}. \tag{20}$$

We focus on half of one side of the shear plot because it is symmetrical and can write Equ. (19). We now plug Equ. (19) into Equ. (18) and integrate. Next we substitute $x = \frac{w}{2}$ and $M(x) = 2M_{CR}$ to get Equ. (20).

$$M_{CR} = \frac{w(N\mu - (m_r + m_e)g|sin\theta|)}{4}. \tag{21}$$

From here, we can make another substitution for F_F from Equ. (13). To get our final equation for the moment exerted by the force of friction, the robot's steering servos will need to overpower to steer the wheels successfully. With this, we specified the strength we needed from the steering servos to turn the robot's wheels successfully. With Equ. (21) in mind, we chose to specify servos which output 10.27 Nm of torque ($M_{CR} = 3.608$ Nm).

IV. Field Deployment and Verification

After having engineered and designed the proposed robot, we moved forward with manufacturing and assembly, which was also done by the ARA Lab team at UNR. Once we had finished assembly, we created the low-level and high-level controls for the robot and the GCS discussed in our overall design section. Next, we began field testing to verify the robot's capabilities.

Fig. 10: The robot traveling up a steel beam using each of the steering methods from left to right.

With field testing, we were able to verify that the proposed robot can successfully do what we engineered it to. The robot does not have any issues with sliding and does not topple over when in use, as seen in Fig. 10. Additionally, we were able to successfully swap between steering configurations to change how the robot could navigate the steel surface it was on.

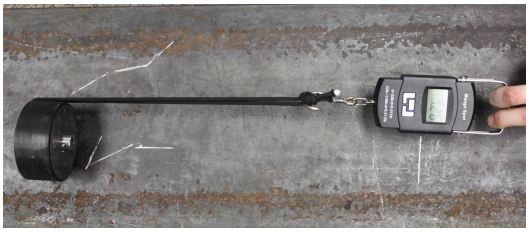

Fig. 11: Testing of the wheels friction with a steel surface.

Next, we decided to create a setup to experimentally determine the required torque to turn the wheels while on steel and see how it measured up to our analysis. Fig. 11 shows how we setup an experiment to determine this. The measured value pulled the wheel right as it began to turn 32.3 N of force at the moment arm of .0318 m. This corresponds to a required torque of 1.23Nm, meaning that our steering servos have an actual FOS of 10.

Using the wheel on steel beam shown in Fig. 11, we also tested the wheels generated friction force against sliding. We found that our equipment was not rated for forces this large but is certain that it performs close to how we predicted mathematically. When testing, the steel beam started sliding on the ground from the pull force we were yanking on the wheel with.

The deployment of the proposed robot can be seen in the video in this link: `https://youtu.be/DqTnZh-fm70`

V. Conclusion and Future Work

This paper discusses the details behind the mechanical design work that goes into creating the proposed robots. As such, the mathematical development of each of our analyses is laid out and discussed in detail. The ARA Lab has engineered, manufactured, assembled, and programmed its next-generation robot specializing in being agile and reliable. The robot can utilize its four independent wheel subsystems in a variety of steering configurations, can travel over 90° internal and external edges, travel on curved members and at its base, and can gather visual data of the area traverses. The significant advantage of this robot is that it will support the additional mass of new equipment for the user to equip it with. This allows the robot the potential to gather many different types of detailed data depending on what additional equipment its users provide to it.

References

[1] H. Ahmed, H. M. La, and N. Gucunski. Review of non-destructive civil infrastructure evaluation for bridges: State-of-the-art robotic platforms, sensors and algorithms. *Sensors*, 20(14), 2020.

[2] S. T. Nguyen and H. M. La. Development of a steel bridge climbing robot. In *2019 IEEE/RSJ International Conference on Intelligent Robots and Systems (IROS)*, pages 1912–1917, 2019.

[3] S. T. Nguyen and H. M. La. A climbing robot for steel bridge inspection. *Journal of Intelligent and Robotic Systems*, 102(75), 2021.

[4] U.S Department of Transportation Highway Administration, National Bridge Inventory Data, 2019. `http://www.fhwa.dot.gov/bridge/nbi.cfm`.

[5] ASCE. 2017 infrastructure report card. `https://www.infrastructurereportcard.org/wp-content/uploads/2017/01/Bridges-Final.pdf`, 2017.

[6] M. Caputo. The economic cost of the bridge collapse. 2007.

[7] P. Ward, P. Manamperi, P. R. Brooks, P. Mann, W. Kaluarachchi, L. Matkovic, G. Paul, C. H. Yang, P. Quin, D. Pagano, D. Liu, K. Waldron, and G. Dissanayake. Climbing robot for steel bridge inspection: Design challenges. In *Austroads Publications Online, ARRB Group*, 2015.

[8] S. T. Nguyen, A. Q. Pham, C. Motley, and H. M. La. A practical climbing robot for steel bridge inspection. In *2020 IEEE International Conf. on Robotics and Automation (ICRA)*, pages 9322–9328, 2020.

[9] H. D. Bui, S. Nguyen, U. H. Billah, C. Le, A. Tavakkoli, and H. M. La. Control framework for a hybrid-steel bridge inspection robot. In *2020 IEEE/RSJ International Conference on Intelligent Robots and Systems (IROS)*, pages 2585–2591, 2020.

[10] M. Eich and T. Vögele. Design and control of a lightweight magnetic climbing robot for vessel inspection. In *the 19th Mediterranean Conf. on Control Automation*, pages 1200–1205, June 2011.

[11] Helical Robotics. Climbing robots for wind turbine inspection. 2013.

[12] F. Tâche, W. Fischer, G. Caprari, R. Siegwart, and R. Moser andF. Mondada. Magnebike : A magnetic wheeled robot with high mobility for inspecting complex-shaped structures,. *Journal of Field Robotics*, 26(5):453–476, Dec 2009.

[13] Haruhiko Eto and H. Harry Asada. Development of a wheeled wall-climbing robot with a shape-adaptive magnetic adhesion mechanism,. *2020 IEEE International Conference on Robotics and Automation (ICRA)*.

[14] A. Pham, C. Motley, S. T. Nguyen, and H. M. La. A robust and reliable climbing robot for steel structure inspection. In *2022 IEEE/SICE International Symposium on System Integration (SII), Narvik, Norway, January 8-12*, 2022.

[15] Illah Nourbakhsh R. Siegwart, EPFL. *Introduction to Autonomous Mobile Roboitcs*. 2011.

[16] AZoM. Aisi 1018 mild/low carbon steel, mechanical properties. 2012.

[17] AZoM. Emulsion polymerised styrene butadiene rubber (e-sbr) – mechanical, electrical and cure properties and resistance to fluids. 2003.

[18] MATWeb. Astm a36 steel material properties.

[19] J. I. Craig O. A. Bauchau. Structural analysis. 2009.